Mathematical Models and Numerical Simulations for the America's Cup

Nicola Parolini *

CMCS, Institut d'Analyse et Calcul Scientifique, EPFL, Lausanne, Switzerland

Alfio Quarteroni

CMCS, Institut d'Analyse et Calcul Scientifique, EPFL, Lausanne, Switzerland
MOX, Dipartimento di Matematica, Politecnico di Milano, Milan, Italy

Abstract

This paper presents a review of the mathematical models which can be adopted to describe the different physical phenomena characterizing the flow around a sailing yacht. The complete model accounting for laminar-turbulent transition regime, free-surface dynamics and fluid-sails interaction is introduced as long as some simplified models that have been used to reduce the computational complexity. Drawing on the experience of the Ecole Polytechnique Fédérale de Lausanne (EPFL) as Official Scientific Advisor to the Alinghi Team, winner of the 2003 America's Cup, we discuss the role of Computational Fluid Dynamics simulations based on Reynolds Averages Navier–Stokes (RANS) equations and their integration in standard yacht design process. Numerical results in different areas (appendages design, free-surface flows, aerodynamics of sails) are presented and discussed.

Key words: Mathematical Modelling, Numerical Fluid Dynamics, Fluid-Structure Interaction, Free-Surface Flows, Yacht Design, America's Cup

1 Introduction

The America's Cup is a yachting race first run in 1851 and whose prize represents the world's oldest sporting trophy. America's Cup yacht races are fiercely competitive. Even after a race of several hours, just seconds can separate two

* Corresponding author. Tel.: +41 21 693 2909; fax.: +41 21 693 4303.
E-mail address: nicola.parolini@epfl.ch

teams at the finish line. Unlike aerospace or automotive applications, for which vast safety margins must be guaranteed, America's Cup competition demands the utmost performance. Design teams must perform extensive analysis to ensure that their racing yachts can pursue victory without slipping over the edge into disaster.

The 31st America's Cup series held this past spring in Auckland, New Zealand, was won by Team Alinghi of Geneva. To help wring every drop of performance out of the latest technology, in July 2001 the Alinghi syndicate named the Federal Institute of Technology in Lausanne (l'Ecole Polytechnique Fédérale de Lausanne, or EPFL) as its official scientific advisor.

Experienced sailors, disciplined training sessions, focused teamwork, and top quality construction all play major roles in the winning of America's Cup class races. But Team Alinghi has also given careful attention to scientific innovation and technical detail in its partnership with the EPFL. Using their prowess in multiple disciplines, the EPFL researchers helped the Alinghi team evaluate commercial materials, developed new materials and methods, and modeled and simulated innovative designs. Their work clearly bore results, because Alinghi sailed under demanding conditions without any perceptible equipment failures. Fifteen senior scientists, drawn especially from two disciplines - polymer technology and applied mathematics, together with some 20 students, have been working in the research, design, construction, outfitting and modification of the Alinghi boats.

2 New materials and complex flowfields, testing and numerical simulation

In addition to getting the departments to function smoothly together as they took their firstrough concepts from design to fabrication, the challenges of the EPFL researchers were technological: developing composite structures to handle extreme conditions, testing the material's resistance to more than the standard 50 tons of pressure applied to the mast under normal conditions at sea, and working out quality-control methods by computer simulation of hundreds of sail and hull profiles. One challenge facing researchers who specialize in sports is the rate of change. In aerospace it takes roughly 10 years to test and validate a new technology, which then has a useful lifetime of at least 20 years. In the automotive industry, the test-and-validation phase is five years with a production lifetime of 12 to 15 years. In sports, however, the length of both the test and usage period runs from 1 to 2 years. Consider how quickly materials and consumer tastes change in tennis rackets, golf clubs, protective sports clothing, running shoes – or racing cars, bicycles or yachts.

Computer simulation was critically important in designing Alinghi below the water line as well as in the air. Mathematical modeling and numerical simulation have been used to reproduce on the computer the complex flow dynamics under a broad variety of sailing conditions, while fluid mechanicists developed detailed flow measurements for the underwater elements, the mast, and the rigging.

Experimental tests in laboratory and in navigation can supply important information on the flow around the boat. Measuring the free-stream turbulence level and detecting laminar-turbulent transition in the boundary layer of the keel and of the bulb is of paramount importance when devising mathematical models for numerical simulation . To experimentally determine the laminar-turbulent transition line on a full-scale training boat under different sailing conditions, a series of sensors on the underwater boat components were mounted.

A statistical analysis of the skin friction fluctuations finally indicate whether the flow is laminar or turbulent. The main challenges were to arrange correctly the array of sensors on the keel to avoid interference between sensors, to separate boat motion from turbulence during data analysis, and to characterize the transition location in a statistical sense (as the transition location constantly moves around on a moving boat). In practice, it was also necessary to distinguish between the output of a malfunctioning sensor (e.g. corroded connections) and turbulence. For all this, digital filtering techniques and statistical data analysis have been carried out, taking advantage of the fact that the frequencies of turbulent fluctuations are generally high with respect to boat motion. Another important source of drag is flow separation from the hull and the sails. This phenomenon is due to fluid particles that no longer follow the surface of the hull or sail and thereby create regions of low-pressure backwash that "hold" the boat back. One area particularly prone to separation is the trim tab that is located on the trailing edge of the keel. This trim tab is angled to increase the lift of the keel, which counteracts the wind's tendency to push the boat sideways.

2.2 Materials

In designing a boat, weight vs. strength is a key design trade-off. A boat makes most efficient use of the wind if it stays as upright as possible because it then exposes more sail area to the wind. To keep the boat upright, the builders try to place as much weight as possible in the bulb. Every kilogram saved on the

hull was shifted 4 meters underwater to the lead-filled bulb to improve speed and stability.

An International America's Cup Class (IACC) boat has a race weight of some 25 tons, of which about 20 are in the underwater lead bulb. Placing weight high above the water line, such as in the mast, is counterproductive. A light mast must nonetheless be extremely strong. In high wind conditions, the standing rigging on such a boat can experience 20 tons of tension, which pulls the mast down toward the hull with a compression force in the range of 50 tons. Not only must the mast not snap under these forces, the hull must be very stiff so it will not buckle in the middle due to these enormous forces. Composite materials represent the most adequate choice to satisfy these requirements of lightness and stiffness. They have been employed for the construction of both hull and mast. In particular, the hull have been realized with a sandwich structure composed by two skins of carbon fiber composite material glued to a light honeycomb core. As material breakage is a constant threat in the extreme conditions of yacht racing, Alinghi's critical mechanical pieces were tested on a 1:1 scale in EPFL labs to insure their reliability. As previously noticed, in contrast with aircraft engineering, where reliability and safety margins are vast, in America's Cup racing boat speed demands that such margins be kept to a minimum.

After the researchers determined the optimum geometry for various vessel components, the boat builders had to create them. The material of choice for many components is "prepreg", which consists of a fabric of carbon fibers impregnated with epoxy resins. It comes in a pliable form, and it becomes hardened when it is cured under temperature. Applying pressure by curing it in an autoclave reduces the porosity in the material to levels below 1%, enhancing its mechanical qualities. America's Cup rules, however, allow the use of such a pressure container only for some parts but not for the hull. The reason is cost; an autoclave big enough to hold hull pieces becomes extremely expensive, and this rule allows teams with smaller budgets to compete. Thus, the curing process for the hull uses a vacuum bag at 1 bar (that is, at roughly 1 atm, and 14.5 lbs/in^2)(This restriction doesn't typically exist in industry; with airplanes, for instance, one strives for the best strength, regardless of the expense.) One key task for the EPFL team was to select the prepreg that would produce the best results under a vacuum-bag environment, determine the optimum curing cycle (how much heat for how long) and create a manufacturing process that the boat builders could easily follow.

3 The mathematical problem and its complexity

One trend that helps explain the importance of technology and testing in the America's Cup is, ironically, uniformity. A decade ago, racing teams experimented with a variety of hull and keel shapes; today, geometries have converged toward standardized shapes, and the smallest details make the difference. Jerome Milgram, veteran of a dozen America's Cup contests and a senior professor at the Massachusetts Institute of Technology, affirmed the importance of fluid dynamics for the design of an America's Cup yacht: "Racing yachts require very high precision in all aspects of the design of the boat and sails. Just a 1% difference in hull resistance leads to a gain or loss at the finish line of more than 30 seconds."

The numerical simulation of the complete flow field around an America's Cup yacht has tremendous computational complexity. It may involve the solution of nonlinear algebraic systems with up to 30 million unknowns to account for the forces of the wind, the waves, and the potential interaction of two boats in the heat of competition. The mathematical equations governing the flow around an International America's Cup Class (IACC) boat have to account for hydrodynamic and aerodynamic flows, wave generation on the water surface, and the interaction of the flow field with the structural components such as the mast and the sails, including the effects from a competitor sailing nearby.

The complexity of the problem considered and the strict time constraints have prompted to the definition of a hierarchy of mathematical models of lower difficulty characterized by different levels of accuracy, complexity, computational cost, ease of use and acceptance within the design community.

3.1 A virtually- intractable mathematical problem

Ideally, a global complete model for IACC boats should be able to reproduce several different aspects of the physical problem. On one hand, to simulate accurately the hydrodynamic and aerodynamic flows around the boat (the hull, the appendages, the mast and the sails), it should account for the viscous effects, the transitional (laminar to turbulent) nature of the flow as well as the wave generation on the water free-surface. On the other hand, the extreme loads acting on the boat (several tons) and the high deformability of the sails make the problem even more difficult, since the deformations induced by the flow on the different components of the boat are relevant.

Let Ω denote the three-dimensional computational domain in which we solve the flow equations. If $\hat{\Omega}$ is a parallelepiped surrounding the boat B, the computational domain is the complementary of B w. r. to $\hat{\Omega}$, $\Omega := \hat{\Omega} \backslash B$ (see

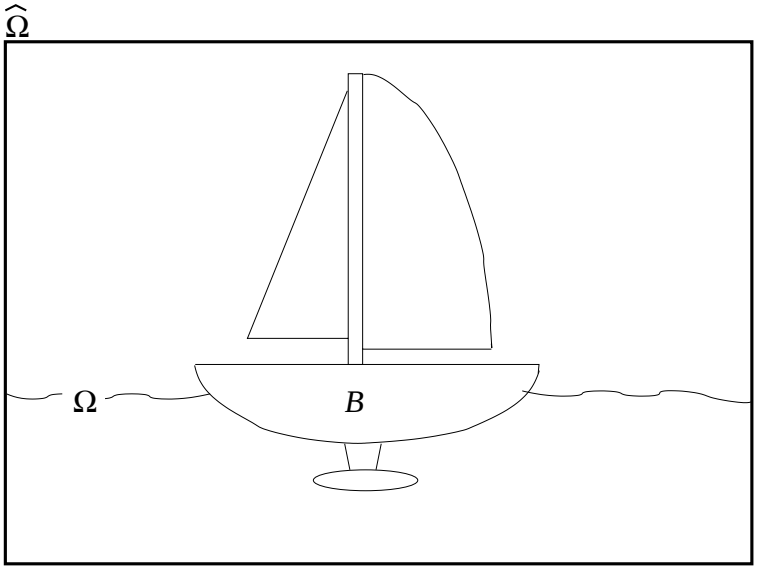

Fig. 1. A two-dimensional section of the computational domain $\Omega = \hat{\Omega} \backslash B$

Fig. 1 for a two-dimensional sketch). In our simulations, $\hat{\Omega}$ features 300 m in the direction of the boat motion, 200 m in the transverse direction, and 180 m vertically. The equations that govern the flow around B are the density-dependent (or inhomogeneous) incompressible Navier–Stokes equations, which read:

$$\frac{\partial \rho}{\partial t} + \boldsymbol{\nabla} \cdot (\rho \boldsymbol{u}) = 0 \tag{1}$$

$$\frac{\partial (\rho \boldsymbol{u})}{\partial t} + \boldsymbol{\nabla} \cdot (\rho \boldsymbol{u} \otimes \boldsymbol{u}) - \boldsymbol{\nabla} \cdot \boldsymbol{T}(\boldsymbol{u}, p) = \rho \boldsymbol{g} \tag{2}$$

$$\boldsymbol{\nabla} \cdot \boldsymbol{u} = 0 \tag{3}$$

for $\boldsymbol{x} \in \Omega$ and $0 < t < T$, and where ρ is the (variable) density, $\boldsymbol{u}$ is the velocity field, p is the pressure, $\boldsymbol{g} = (0, 0, g)^T$ is the gravity acceleration, and $\boldsymbol{T}(\boldsymbol{u}, p) := \mu(\boldsymbol{\nabla u} + \boldsymbol{\nabla u}^T) - p\boldsymbol{I}$ is the stress tensor with μ indicating the (variable) viscosity. Equation (1) translates the principle of mass conservation, equation (2) enforces the conservation of linear momentum, while equation (3) is the constraint of incompressibility.

The above equations have to be complemented with the initial conditions

$$\boldsymbol{u} = \boldsymbol{u}_0, \quad \rho = \rho_0 \quad \text{in } \Omega \text{ at } t = 0, \tag{4}$$

and by suitable boundary conditions

$$\boldsymbol{u} = \boldsymbol{\phi} \quad \text{on } \partial\Omega, 0 < t < T, \tag{5}$$

$$\rho = \rho_{in} \quad \text{on } \{\boldsymbol{x} \in \partial\Omega : \boldsymbol{u} \cdot \boldsymbol{n} < 0\}, 0 < t < T, \tag{6}$$

where $\boldsymbol{n}$ is the unit outward normal on $\partial\Omega$. Further, on the boat boundary ∂B we set $\boldsymbol{u} = 0$ if we consider the boat (and the sails) undeformable, otherwise we refer to the discussion at subsection 3.4 in this section.

In spite of the fact that the Navier-Stokes equations were introduced more than a century ago, around them thousands of mathematicians, physicists and engineers are still striving. Their complete understanding is far from being achieved (indeed, this is one of the 10 unsolved problems which have been endowed with a grant of one million dollars each at the beginning of the third millennium).

A global existence result can be proven for the solution of (1)-(3) provided Ω is a bounded, connected, open subset of $\mathbb{R}^3$ with smooth boundary (the latter condition is not satisfied in the case at hand, indeed ∂B is only Lipschitz-continuous). In that case, if $\rho_0 \in L^\infty(\Omega)$ and $\boldsymbol{u}_0 \in (H^1(\Omega))^3$, $\boldsymbol{m}_0 := \rho\boldsymbol{u}|_{t=0} \in L^\infty(\Omega)$ then a weak solution exists which satisfies

$$\begin{aligned} \rho &\in L^\infty(0,T;L^\infty(\Omega)), \\ \boldsymbol{u} &\in L^2(0,T;H_0^1(\Omega))^3, \\ \rho|\boldsymbol{u}|^2 &\in L^\infty(0,T;L^1(\Omega)), \\ \boldsymbol{\nabla u} &\in L^2(\Omega \times (0,T)), \\ \rho &\in C([0,T];L^p(\Omega)), \quad \forall \quad 1 \le p < \infty \end{aligned} \tag{7}$$

(see [11]). Moreover, the following energy inequalities hold

$$\frac{d}{dt}\int_\Omega \rho|\boldsymbol{u}|^2\,d\boldsymbol{x} + \int_\Omega \mu(\partial_i u_j + \partial_j u_i)^2\,d\boldsymbol{x} \le 2\int_\Omega \rho\boldsymbol{g}\cdot\boldsymbol{u}\,d\boldsymbol{x} \quad \text{in } \mathcal{D}'(0,T) \tag{8}$$

$$\int_\Omega \rho|\boldsymbol{u}|^2\,d\boldsymbol{x} + \int_0^t\int_\Omega \mu(\partial_i u_j + \partial_j u_i)^2\,d\boldsymbol{x}\,ds \le \int_\Omega |\boldsymbol{m}_0|^2/\rho_0\,d\boldsymbol{x} + 2\int_0^t\int_\Omega \rho\boldsymbol{g}\cdot\boldsymbol{n}\,d\boldsymbol{x}\,ds \quad \text{a.e. } t \in (0,T), \tag{9}$$

where ∂_i denotes partial derivative w. r. to x_i, $\mathcal{D}'(0,T)$ is the space of distributions on $(0,T)$ and summation convention on repeated indexes applies.

Uniqueness of weak solution is known to be an open problem; however, any weak solution is equal to a strong solution if the latter exists. Uniqueness is closely related to the regularity of solutions. In this respect, there isn't any further meaningful regularity result on $\boldsymbol{u}$ and ρ other than what stated in (7), in particular very little is known on the pressure field p (which acts as a Lagrange multiplier in (2)-(3)). Special considerations apply when Ω is a two-dimensional domain and the viscosity μ is a positive constant which does not depend on ρ, see [11], a circumstance which has little in common with our problem, though.

3.2 Free-surface flows

In the case we are interested in, the computational domain Ω is made of two components, the volume Ω_w occupied by the water and that Ω_a occupied by the air. The interface Γ separating Ω_w from Ω_a is the (unknown) free-surface, which may be a disconnected two-dimensional manifold if wave breaking is accounted for. The unknown density ρ actually takes two constant states, ρ_w (in Ω_w) and ρ_a (in Ω_a). The values of ρ_w and ρ_a depend on the fluid temperatures, which are considered to be constant in the present model. The fluid viscosities μ_w (in Ω_w) and μ_a in (Ω_a) are constants which depend on ρ_w and ρ_a, respectively.

The set of equations (1)-(3) can therefore be seen as a model for the evolution of a two-phase flow consisting of two immiscible incompressible fluids with constant densities ρ_w and ρ_a and different viscosity coefficients μ_w and μ_a. In this respect, in view of the numerical simulation, we could regard equation (1) as the candidate for updating the (unknown) interface location Γ, then treat equations (2)-(3) as a coupled system of Navier–Stokes equations in the two sub-domains Ω_w and Ω_a:

$$\frac{\partial(\rho_w \boldsymbol{u}_w)}{\partial t} + \boldsymbol{\nabla}\cdot(\rho_w \boldsymbol{u}_w \otimes \boldsymbol{u}_w) - \boldsymbol{\nabla}\cdot\boldsymbol{T}_w(\boldsymbol{u}_w, p_w) = \rho_w \boldsymbol{g},$$

$$\boldsymbol{\nabla}\cdot\boldsymbol{u}_w = 0,$$

in $\Omega_w \times (0,T)$,

$$\frac{\partial(\rho_a \boldsymbol{u}_a)}{\partial t} + \boldsymbol{\nabla}\cdot(\rho_a \boldsymbol{u}_a \otimes \boldsymbol{u}_a) - \boldsymbol{\nabla}\cdot\boldsymbol{T}_a(\boldsymbol{u}_a, p_a) = \rho_a \boldsymbol{g},$$

$$\boldsymbol{\nabla}\cdot\boldsymbol{u}_a = 0,$$

in $\Omega_a \times (0,T)$. We have set $\boldsymbol{T}_w(\boldsymbol{u}_w, p_w) := \mu_w(\boldsymbol{\nabla}\boldsymbol{u}_w + \boldsymbol{\nabla}\boldsymbol{u}_w{}^T) - p_w\boldsymbol{I}$, while $\boldsymbol{T}_a(\boldsymbol{u}_a, p_a)$, is defined similarly.

The free surface Γ is a sharp interface between Ω_w and Ω_a. Since there is no flow through it, the normal components of the two velocities $\boldsymbol{u}_a \cdot \boldsymbol{n}$ and $\boldsymbol{u}_w \cdot \boldsymbol{n}$ should agree on Γ. Furthermore, the tangential components must match as well since the two flows are incompressible. Thus we have the following kinematic condition

$$\boldsymbol{u}_a = \boldsymbol{u}_w \quad \text{on } \Gamma. \tag{10}$$

Moreover, the forces acting on the fluid at the free-surface are in equilibrium. This is a dynamic condition and means that the normal forces on either side of Γ are of equal magnitude and opposed direction, while the tangential forces must agree in both magnitude and direction:

$$\boldsymbol{T}_a(\boldsymbol{u}_a, p_a) \cdot \boldsymbol{n} = \boldsymbol{T}_w(\boldsymbol{u}_w, p_w) \cdot \boldsymbol{n} + \kappa\sigma\boldsymbol{n} \quad \text{on } \Gamma, \tag{11}$$

where σ is the surface tension coefficient, that is a force per unit length of a free surface element acting tangential to the free-surface. It is a property of the liquid and depends on the temperature as well as on other factors. The quantity κ in (11) is the curvature of the free-surface, $\kappa = R_{t_1}^{-1} + R_{t_2}^{-1}$, where R_{t_1} and R_{t_2} are radii of curvature along the coordinates (t_1, t_2) of the plane tangential to the free-surface (orthogonal to $\boldsymbol{n}$).

3.3 Modelling the turbulence

The flow around a IACC boat in standard race regime exhibits turbulent behaviour over the vast majority of the yacht surface. Turbulent flows are characterized by being highly unsteady, three-dimensional, containing vortices and coherent structures which stretch and increase the intensity of turbulence. Even more importantly, they fluctuate on a broad range of scales (in space and time). This feature makes the so-called direct numerical simulation (DNS) unaffordable. By DNS we mean the numerical solution of Navier–Stokes equations by a computational grid fine enough to allow that all the significant structures of the turbulence have been captured.

This would require the computational domain to be at least as large as the largest turbulent eddy, the latter being of the order of few times the linear length of the sailing boat. On the other hand, a simulation should capture all of the kinetic energy dissipation, which occurs on the smallest scale whose size η has been determined by Kolmogoroff.

It turns out that in a DNS the number of gridpoints in each direction must be at least L/η, but this ratio is proportional to $Re_L^{3/4}$, where Re_L is the Reynolds number based on the magnitude of the velocity fluctuations. (In our problem, the Reynolds number is of the order of 10^6.)

In the three-dimensional computational domain the total number of gridpoints

should therefore scale as $Re_L^{9/4}$, a number which becomes easily prohibitive due to the limitations on computer speed and memory.

Reynolds averaged Navier–Stokes (RANS) models move from the idea of decomposing the velocity components u_i, the pressure p and the density ρ into a mean part and a fluctuating part

$$p = \bar{p} + p', \quad \rho = \bar{\rho} + \rho', \quad u_i = \bar{u}_i + u_i', \quad i = 1, 2, 3$$

where the overbar denotes the Reynolds average, also called filter. The latter can be operated in a variety of ways, such as the Fourier filter (which is the truncation at a suitable order of the Fourier series of a function), statistical average, time average for a statistically steady turbulence, volume average for a statistically homogeneous turbulence, or ensemble (space-time) average in a more general case.

Operating the average on the Navier–Stokes equations (1)-(3) and assuming that the filter satisfies the following properties

(i) *linearity*

$$\overline{u + \lambda v} = \bar{u} + \lambda \bar{v}, \qquad \forall \lambda \in \mathbb{C},$$

(ii) *derivatives and averages commutation*

$$\overline{\partial_x u} = \partial_x \bar{u},$$

(iii) *double average* (filters have no effect on filtered variables)

$$\bar{\bar{u}} = \bar{u},$$

(iv) *product average*

$$\overline{u\bar{v}} = \bar{u}\bar{v},$$

we obtain:

$$\partial_t \bar{\rho} + \tilde{\boldsymbol{u}} \cdot \boldsymbol{\nabla} \bar{\rho} = 0 \tag{12}$$

$$\partial_t(\bar{\rho}\tilde{\boldsymbol{u}}) + \boldsymbol{\nabla} \cdot (\bar{\rho}\tilde{\boldsymbol{u}} \otimes \tilde{\boldsymbol{u}}) - \boldsymbol{\nabla} \cdot \boldsymbol{T}_{\bar{\mu}}(\bar{\boldsymbol{u}}, \bar{p}) = \rho \boldsymbol{g} + \boldsymbol{\nabla} \cdot (\widetilde{R} + S) \tag{13}$$

$$\boldsymbol{\nabla} \cdot \bar{\boldsymbol{u}} = 0. \tag{14}$$

Here $\tilde{\boldsymbol{u}} := \bar{\rho}\,\bar{\boldsymbol{u}}/\rho$ is the so-called Favre average, while $\widetilde{R}$ represents the Reynolds stress tensor

$$\widetilde{R_{ij}} = -\bar{\rho}\widetilde{u_i'' u_j''} = -\overline{\rho u_i'' u_j''}, \quad i, j = 1, 2, 3 \tag{15}$$

with $\tilde{\boldsymbol{u}}'' = \boldsymbol{u} - \tilde{\boldsymbol{u}}$; finally, the extra stress $S_{ij} = \overline{\mu' \partial_j \boldsymbol{u}_i'}$, $i, j = 1, 2, 3$, is due to the fact that μ is not constant (for this derivation see e.g. Mohammadi–Pironneau [16]).

The new system of equations must be closed by introducing a suitable representation (or model) of the Reynolds stresses. This can be done by resorting to several strategies. One way (which is quite popular in the engineering community) is to express them in terms of two additional quantities, the turbulent kinetic energy k and its dissipation rate ε, using the so-called Boussinesq hypothesis. The two extra (closure) equations have to be added in order to determine the unknown variables k and ε. A complete derivation for the general case is long and tedious. A simpler form can be obtained when both ρ and μ are constant. This is actually the case when a domain decomposition approach is adopted, restricting the equations to the two sub-domains Ω_w and Ω_a (wherein density and viscosity are constant) and introducing suitable interface conditions (see Section 3.2). The formulation for the problem with constant coefficients (in either Ω_a or Ω_w) is reported here for reader's convenience:

$$\begin{aligned} \partial_t(\bar{\rho}\bar{\boldsymbol{u}}) + \boldsymbol{\nabla}\cdot(\bar{\rho}\bar{\boldsymbol{u}}\otimes\bar{\boldsymbol{u}}) + \boldsymbol{\nabla}p^\star - \\ \boldsymbol{\nabla}\cdot[(\mu+\mu_T)(\boldsymbol{\nabla}\bar{\boldsymbol{u}} + \boldsymbol{\nabla}\bar{\boldsymbol{u}}^T)] = \rho\boldsymbol{g} \end{aligned} \tag{16}$$

$$\boldsymbol{\nabla}\cdot\bar{\boldsymbol{u}} = 0, \tag{17}$$

where $\mu_T = \rho\nu_T$, $\nu_T = C_\mu k^2/\varepsilon$ is the (modelled) turbulent viscosity, $p^\star = \bar{p} + 2/3\rho k$. The equations for k and ε read:

$$\partial_t k + \boldsymbol{u}\cdot\boldsymbol{\nabla}k - \boldsymbol{\nabla}\cdot(\nu_T\boldsymbol{\nabla}k) - \nu_T E + \varepsilon = 0 \tag{18}$$

$$\partial_t\varepsilon - \boldsymbol{\nabla}\cdot(\frac{C_\varepsilon}{C_\mu}\nu_T\boldsymbol{\nabla}\varepsilon) - C_1 kE + C_2\frac{\varepsilon^2}{k} = 0 \tag{19}$$

where $E = 1/2|\boldsymbol{\nabla}\bar{\boldsymbol{u}} + \boldsymbol{\nabla}\bar{\boldsymbol{u}}^T|^2$ and being C_μ, C_ε, C_1 and C_2 suitable constants ("magic" numbers are $C_\mu = 0.09$, $C_\varepsilon = 0.126$, $C_1 = 1.92$ and $C_2 = 0.07$). The physical meaning of ε and k is $k = \frac{1}{2}|\bar{\boldsymbol{u}'}|^2$ and $\varepsilon = \frac{\mu}{2\rho}\overline{|\boldsymbol{\nabla}\boldsymbol{u}' + \boldsymbol{\nabla}\boldsymbol{u}'^T|^2}$. All variables should indeed be denoted by the underscript "a" in Ω_a or "w" in Ω_w.

3.4 Sail deformation and fluid-sail interaction

A further set of equations should be considered to account for the sail deformation. We denote by S_t the current configuration of the sail at time t and by $S_0 \subset \mathbb{R}^3$ its initial configuration that we suppose unstressed.

Let $\boldsymbol{f}$ be the body force exerted on the sail (e.g. the gravity) and ρ_s its density. The equilibrium equations which govern the sail deformation in the

three-dimensional elastodynamics framework read

$$\rho_s \partial_{tt} \boldsymbol{\psi} - \boldsymbol{\nabla} \cdot (\boldsymbol{\sigma}(\boldsymbol{\psi})) = \boldsymbol{f}, \quad \text{in } S_0 \times \mathbb{R}^+, \tag{20}$$

where $\boldsymbol{\psi} : S_0 \times \mathbb{R}^+ \to S_t$ is the transformation map which must verify the initial conditions $\boldsymbol{\psi}(\boldsymbol{x}, 0) = \boldsymbol{x}$ and $\partial_t \boldsymbol{\psi}(\boldsymbol{x}, 0) = 0$.

For a Saint-Venant material, $\boldsymbol{\sigma} = \boldsymbol{\sigma}(\boldsymbol{\psi})$ is the second Piola-Kirchhoff stress tensor and takes the following form

$$\boldsymbol{\sigma} = \lambda_s \mathrm{Tr}(\boldsymbol{E}) \boldsymbol{I} + 2\mu_s \boldsymbol{E}, \tag{21}$$

where λ_s and μ_s indicate the Poisson ratio and Young modulus of the sail, $\boldsymbol{E} = \frac{1}{2}(\boldsymbol{\nabla}\boldsymbol{\psi}^T \boldsymbol{\nabla}\boldsymbol{\psi} - \boldsymbol{I})$ is the Green-Saint Venant strain tensor and $\mathrm{Tr}(\boldsymbol{E})$ is its trace.

Boundary conditions have to be provided as well on the sail boundaries. We suppose that the boundary of S_0 is divided into two parts, Γ^D where the sail is fixed and Γ^I is the interface which is in contact with the fluid. It follows that

$$\boldsymbol{\psi}(\boldsymbol{x}, t) = \boldsymbol{x}, \quad (\boldsymbol{x}, t) \in \Gamma^D \times \mathbb{R}^+. \tag{22}$$

In addition, we have two coupling conditions. The former is given by

$$\partial_t \boldsymbol{\psi}(\boldsymbol{x}, t) = \boldsymbol{u}(\boldsymbol{\psi}(\boldsymbol{x}, t), t), \quad (\boldsymbol{x}, t) \in \Gamma^I \times \mathbb{R}^+, \tag{23}$$

which means that the velocity fields are continuous at the interface. The latter, which expresses the continuity of the stress vectors at the interface, is given by

$$(\boldsymbol{\nabla}\boldsymbol{\psi}\boldsymbol{\sigma}) \cdot \boldsymbol{n}_S = [(\boldsymbol{T}(\boldsymbol{u}, p) \circ \boldsymbol{\psi}) \, \mathrm{Cof}(\boldsymbol{\nabla}\boldsymbol{\psi})] \cdot \boldsymbol{n}_S, \quad \text{on } \Gamma^I \times \mathbb{R}^+, \tag{24}$$

where $\boldsymbol{n}_S$ is the unit normal vector on Γ^I, $\mathrm{Cof}(\boldsymbol{\nabla}\boldsymbol{\psi}) = \mathrm{Det}(\boldsymbol{\nabla}\boldsymbol{\psi})\boldsymbol{\nabla}\boldsymbol{\psi}^{-T}$ the cofactor tensor and $\boldsymbol{T}(\boldsymbol{u}, p)$ the Cauchy stress tensor of the fluid. If $\boldsymbol{\Sigma}$ is a tensor and $\boldsymbol{n}$ a vector, $\boldsymbol{\Sigma} \cdot \boldsymbol{n}$ denotes the vector whose i-th component is $\boldsymbol{\Sigma}_{ij}\boldsymbol{n}_j$ (sum on j).

It is convenient to make use of a reference domain as well, that we denote Ω_S. Each point $\boldsymbol{x} \in S_0$ is represented through the map $\boldsymbol{\Phi}_0 : \Omega_S \to S_0$, $\boldsymbol{\xi} \to \boldsymbol{x} = \boldsymbol{\Phi}_0(\boldsymbol{\xi})$. The transformation map $\boldsymbol{\Phi} : \Omega_S \times \mathbb{R}^+ \to S_t$ is defined as follows

$$\boldsymbol{\Phi}(\boldsymbol{\xi}, t) = \boldsymbol{\psi}(\boldsymbol{\Phi}_0(\boldsymbol{\xi}), t). \tag{25}$$

Transported on Ω_S, the equation (20) reads

$$\rho_0 \partial_{tt} \boldsymbol{\Phi} - \boldsymbol{\nabla} \cdot (\boldsymbol{\nabla}\boldsymbol{\Phi}\boldsymbol{\sigma}_0) = \boldsymbol{f}_0, \quad \text{in } \Omega_S \times \mathbb{R}^+, \tag{26}$$

where $\rho_0 = \rho_s \mathrm{Det}(\boldsymbol{\nabla}\boldsymbol{\Phi}_0)$, $\boldsymbol{f}_0 = \boldsymbol{f}\mathrm{Det}(\boldsymbol{\nabla}\boldsymbol{\Phi}_0)$ and

$$\boldsymbol{\sigma}_0 = \boldsymbol{\nabla}\boldsymbol{\Phi}_0^{-1} \boldsymbol{\sigma} \mathrm{Cof}(\boldsymbol{\nabla}\boldsymbol{\Phi}_0). \tag{27}$$

Let us denote by Γ_0^D and Γ_0^I the corresponding boundary conditions on Ω_S such that $\mathbf{\Phi}_0(\Gamma_0^D) = \Gamma^D$ and $\mathbf{\Phi}_0(\Gamma_0^I) = \Gamma^I$. Then, the boundary condition (22) becomes

$$\mathbf{\Phi}(\boldsymbol{\xi}, t) = \mathbf{\Phi}_0(\boldsymbol{\xi}), \quad (\boldsymbol{\xi}, t) \in \Gamma_0^D \times \mathbb{R}^+, \tag{28}$$

and the two coupling boundary conditions (23) and (24) read

$$\boldsymbol{u}(\mathbf{\Phi}(\boldsymbol{\xi}, t), t) = \partial_t \mathbf{\Phi}(\boldsymbol{\xi}, t), \quad (\boldsymbol{\xi}, t) \in \Gamma_0^I \times \mathbb{R}^+, \tag{29}$$

$$(\boldsymbol{\nabla}\mathbf{\Phi}\boldsymbol{\sigma}_0) \cdot \boldsymbol{n}_0^S = [(\boldsymbol{T}(\boldsymbol{u}, p) \circ \mathbf{\Phi})\,\mathrm{Cof}(\boldsymbol{\nabla}\mathbf{\Phi})] \cdot \boldsymbol{n}_0^S, \quad \text{on } \Gamma_0^I \times \mathbb{R}^+. \tag{30}$$

Since sails are thin structures, several assumptions can be made in order to reduce the general three-dimensional elastic model equations (20)-(21) to a two-dimensional shell model. The reference domain Ω_S can be described as a thin parallelepipedal domain of $\mathbb{R}^3$ whose coordinates are (ξ_1, ξ_2, z), with $(\xi_1, \xi_2) \in \omega \subset \mathbb{R}^2$ and $-h/2 \leq z \leq h/2$, h being the shell thickness. In its initial configuration S_0 the sail is described as

$$\mathbf{\Phi}_0(\xi_1, \xi_2, z) = \boldsymbol{\varphi}_0(\xi_1, \xi_2) + z\boldsymbol{t}_0(\xi_1, \xi_2), \tag{31}$$

where $\boldsymbol{\varphi}_0 : \omega \to \mathbb{R}^3$ is the parametrization of the middle surface of S_0 and $\boldsymbol{t}_0$ its unit normal vector which is defined as

$$\boldsymbol{t}_0 = \frac{\partial_1\boldsymbol{\varphi}_0 \times \partial_2\boldsymbol{\varphi}_0}{\|\partial_1\boldsymbol{\varphi}_0 \times \partial_2\boldsymbol{\varphi}_0\|}, \tag{32}$$

where $\times$ denotes the cross product of $\mathbb{R}^3$ and $\|\cdot\|$ the $L^2(\omega)$ norm.

To derive the two-dimensional shell model, it is assumed that the deformed configuration S_t of the sail is described as

$$\mathbf{\Phi}(\xi_1, \xi_2, z; t) = \boldsymbol{\varphi}(\xi_1, \xi_2; t) + z\boldsymbol{t}(\xi_1, \xi_2; t), \tag{33}$$

where $\boldsymbol{\varphi} : \omega \to \mathbb{R}^3$ is the parametrization of the middle surface of S_t and $\boldsymbol{t}$ its unit normal vector. Furthermore, the stresses are assumed to be plane. However, the latter hypothesis is in contradiction with (33) since the normal fibers are supposed inextensible. This controversy is resolved at the expense of modifying the constitutive law (21) as follows

$$\boldsymbol{\sigma} = \lambda_s^* \mathrm{Tr}(\boldsymbol{E})\boldsymbol{I} + 2\mu_s\boldsymbol{E}, \quad \text{with } \lambda_s^* = \frac{2\lambda_s\mu_s}{\lambda_s + 2\mu_s}. \tag{34}$$

Therefore, in this context the hypothesis of inextensibility of the normal fibers is not physical. The fiber can deform in the real displacement.

The Navier–Stokes equations (in their RANS form) together with the structure equation (26)-(27)-(34) and the coupling conditions (29)-(30) provide a globally coupled, fluid-structure problem.

4 On the numerical discretization

In this section, we give an overview on the numerical schemes adopted for the discrete solution of the mathematical problems introduced in Section 3.

4.1 Numerical discretization of flow equations

The spatial discretization of the Navier–Stokes equations (1)-(3) is based on a cell-centered finite-volume approach on unstructured grids. The governing equations are integrated over suitable control volumes yielding discrete equations that conserve each quantity on a control-volume base. Then a SIMPLE like strategy [14] is used to decouple the pressure computation from the computation of the velocity field. The same kind of finite volume discretization has been adopted for the solution of the $k-\varepsilon$ turbulence equations.

For reader's convenience, let us recall the general principles behind finite volumes introducing the discretization of a simple steady advection-diffusion for a scalar quantity ψ:

$$-\boldsymbol{\nabla}\cdot(\mu\,\boldsymbol{\nabla}\psi-\rho\,\boldsymbol{u}\,\psi)=S,\qquad\text{in }\Omega, \tag{35}$$

where ρ is a given scalar function (say, the density), $\boldsymbol{u}$ is a given convective field, μ is a non-negative diffusion coefficient and S is a source term per unit volume. For an arbitrary control volume $c\subset\Omega$, the Gauss theorem yields:

$$\oint_{\partial c}\rho\,\psi\,\boldsymbol{u}\cdot\boldsymbol{n}\,d\Gamma=\oint_{\partial c}\mu\,\boldsymbol{\nabla}\psi\cdot\boldsymbol{n}\,d\Gamma+\int_c S\,dV, \tag{36}$$

where $\boldsymbol{n}$ is the outward unit normal vector on the control volume boundary ∂c. The discretization of equation (36) on a given cell c (now cell stands for control volume) reads

$$\sum_f^{N_{\text{faces}}}\rho_f\,\psi_f\,\boldsymbol{u}_f\cdot\boldsymbol{n}_f\,|A_f|=\sum_f^{N_{\text{faces}}}\mu_f\,(\boldsymbol{\nabla}\psi)_f\cdot\boldsymbol{n}_f\,|A_f|+S\,|V_c|, \tag{37}$$

where the index f represents quantities evaluated on a given face f, N_{faces} is the number of faces of the cell contour, $|A_f|$ is the area of face f and $|V_c|$ is the measure (volume) of cell c. Within a given cell, all the quantities are supposed to be constant and their constant value is identified with the pointwise value at the cell center of gravity. Consequently, the face values need to be suitably defined. Those of the convective terms are typically obtained by an upwind interpolation from the adjacent cell center values. In our computations a second-order upwind scheme based on a multidimensional linear reconstruction approach [1] has been used.

For the diffusion terms in equation (37) a second-order accurate central scheme is used. The face value for a variable ψ is defined as follows:

$$\psi_f = \frac{1}{2}(\psi_0 + \psi_1) + \frac{1}{2}(\boldsymbol{\nabla}\psi_{r,0} \cdot \boldsymbol{r}_0 + \boldsymbol{\nabla}\psi_{r,1} \cdot \boldsymbol{r}_1) \tag{38}$$

where the indices 0 and 1 refer to the cells that share face, $\boldsymbol{\nabla}\psi_{r,0}$ and $\boldsymbol{\nabla}\psi_{r,1}$ are the reconstructed gradients at cells 0 and 1, respectively, and $\boldsymbol{r}$ is the vector directed from the cell centroid toward the face centroid.

The integration of the momentum equation (2) and the equations for the turbulence quantities k and ε (18)-(19) is accomplished by first linearizing the equation at hand, then proceeding like for equation (35).

For every cell, equation (37) boils down to an algebraic equation of the following form:

$$a_c \psi_c = \sum_{nb} a_{nb} \psi_{nb} + b \tag{39}$$

where c is the cell index while the index nb ranges over the neighbor cells, and a_c and a_{nb} are suitable coefficients. This results in a set of algebraic equations with sparse coefficient matrix for the vector $\{\psi_c, c = 1, \cdots, N_c\}$ (with N_c denoting the number of cells).

In most of the simulations carried out in the present work, we have been looking for a steady state solution. In that case, the momentum and continuity equations (1)-(3) can be written in integral form as follows:

$$\oint_{\partial c} \rho\, \boldsymbol{u} \otimes \boldsymbol{u} \cdot \boldsymbol{n}\, d\Gamma - \oint_{\partial c} \boldsymbol{T}(\boldsymbol{u}, p) \cdot \boldsymbol{n}\, d\Gamma = \int_c \rho \boldsymbol{g} dV \tag{40}$$

$$\oint_{\partial c} \rho\, \boldsymbol{u} \cdot \boldsymbol{n}\, d\Gamma = 0. \tag{41}$$

Upon linearization, the finite volume discretization of the x-component of equation (40) yields:

$$a_c u_c = \sum_{nb} a_{nb} u_{nb} + \sum_{f}^{N_{\text{faces}}} p_f\, \boldsymbol{n}_f \cdot \hat{\mathbf{i}}\, |A_f| \tag{42}$$

where $\hat{\mathbf{i}}$ is the unitary vector in the x-direction and the u variable indicates the first component of the vector field $\boldsymbol{u}$. Similar equations hold for the y and z components, however on the latter a source term $-\rho g |V_c|$ shows up on the right hand side.

As previously mentioned, the solution algorithm is based on the SIMPLE method, a pressure-correction iterative numerical scheme for incompressible flows. The basic ideas underlying the SIMPLE method are more easily explained on the algebraic system arising from the discretization of equations

(40)-(41), that reads:

$$\begin{pmatrix} C & G \\ G^T & 0 \end{pmatrix} \begin{pmatrix} U \\ P \end{pmatrix} = \begin{pmatrix} b_1 \\ b_2 \end{pmatrix}, \tag{43}$$

where U and P are the algebraic vectors corresponding to the velocity components and the pressure, respectively. We denote with D the diagonal of matrix C and $R = -G^T C^{-1} G$. Given an initial estimate of the pressure P^*, the SIMPLE method is described by the following iterative algorithm:

(1) Solve $C\tilde{U} = b_1 - G P^*$.
(2) Solve $R P' = b_2 - G^T \tilde{U}$.
(3) Compute $U = \tilde{U} - D^{-1} G P'$ and set $P = P^* + P'$ (note that D^{-1} is used instead of the true inverse C^{-1} to reduce computational complexity).
(4) If not converged, set $P^* = P$ and go to 1.

In the framework of the previous finite volume discretization, each iteration of the SIMPLE method consists in the following steps:

(1) We solve the momentum equations using the value of pressure p^* from previous iteration and velocity, in order to compute an intermediate velocity field $\tilde{\boldsymbol{u}}$ which is not divergence free. Its x-component is:

$$a_c \tilde{u}_c = \sum_{nb} a_{nb} \tilde{u}_{nb} + \sum_{f}^{N_{\text{faces}}} p_f^* \, \boldsymbol{n} \cdot \hat{\mathbf{i}} |A_f|. \tag{44}$$

(2) We denote the new pressure $p = p^* + p'$, p' being a correction. By imposing the mass conservation (41), we find $b_2 = G^T U = G^T C^{-1} (b_1 - G P) = G^T \tilde{U} + R P'$. With the help of a little algebra, this yields the following (Poisson-type) equation for the pressure correction:

$$a_c p'_c = \sum_{nb} a_{nb} p'_{nb} + b_2. \tag{45}$$

The right hand side term b is the net flow rate into the cell, defined as

$$b_2 = \sum_{f}^{N_{\text{faces}}} J_f \, A_f \tag{46}$$

where the face flux J_f is computed using a momentum-weighted average based on the a_c coefficients from equation (42). This is necessary to prevent the checkerboarding that occurs if linear interpolation of cell-centered velocities is used in combination with a collocated scheme (velocity and pressure associated to the same position), as shown by Rhie and Chow [18].

(3) Correcting the cell pressure and face flux

$$p = p^* + \alpha\, p' \tag{47}$$
$$J_f = J_f^* + \beta\, d_f (p'_{c0} - p'_{c1}) \tag{48}$$

where α and β are positive dumping factors between 0 and 1 (which help convergence to the steady state), p'_{c0} and p'_{c1} are the pressure corrections within the two cells on either side of face f and d_f is a function of the average of the momentum equation a_c coefficients for the cells on either side of face f.

The iteration loop is stopped when the convergence criteria, based on the scaled residuals of each equation, are fulfilled.

The solution of the three linear algebraic systems in (44) (one for each velocity component) and the one for the pressure correction in (45) can be accomplished, *e.g.*, by an algebraic multigrid method [6] with Gauss-Seidel smoothing (or else by any Krylov method with suitable preconditioner, see *e.g.*, [17]).

4.2 Numerical approximation of the free-surface

The main problem encountered in the numerical simulation of this kind of flows is the accurate computation of the dynamics of the interface separating the different fluids, since neither the shape nor the position of the interface is known a priori. Numerical methods for the solution of free-surface problems for incompressible viscous flows can be classified in two categories: front-tracking and front-capturing methods.

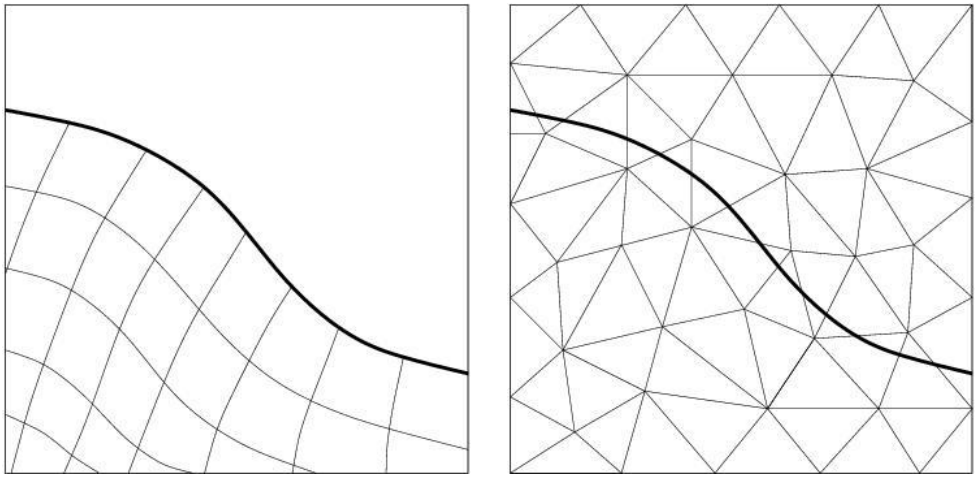

Fig. 2. Typical grid topologies in 2D for Lagrangian (left) and Eulerian (right) free-surface methods. The solid line is the free surface.

Front-tracking methods are based on a Lagrangian approach: the computational grid is adapted to the free-surface, moving and deforming with it [9,23,7,5]. Usually, only the liquid phase is computed and the free surface is treated as a boundary of the computational domain (see Fig. 2, left). The free-surface motion is governed by the a kinematic condition,

$$\frac{\partial \gamma}{\partial t} + u\frac{\partial \gamma}{\partial x} + v\frac{\partial \gamma}{\partial y} = w \tag{49}$$

where $\Gamma = \Gamma(x, y)$ is the height of the free-surface above the static waterplane and u, v and w are the cartesian components of the velocity field. If the viscous shear stresses and the surface tension are neglected, the dynamic free-surface condition 11 can be reduced to a boundary condition on the pressure

$$p = p_{atm} \qquad \text{on } \Gamma, \tag{50}$$

where p_{atm} is the atmospheric pressure. The free-surface boundary is initialized as the static waterplane. As the calculation progresses, the boundary deforms to match the free-surface height given by Γ and the volume grid is deformed consequently. These methods are usually limited to flows with a smooth free-surface, in fact they are able to provide a sharp well-defined interface but encounter difficulties in dealing with interfaces with high deformations or changes of topology (e.g. breaking or overturning waves).

On the other hand, *front-capturing methods* are based on an Eulerian approach: the computational grid is fixed and both the regions occupied by liquid and gas are modelled (see Fig. 2, right). The interface between the different immiscible fluids is "captured" by solving an additional advection equation. The most widely employed front capturing methods for predicting free-surface flows with complex interfaces are the Volume of Fluid (VOF) method [8,10] and the level set method [13,22,12,21,24].

In the VOF method, the location of the interface can be generally obtained by advecting a function $F(\boldsymbol{x}, t)$ representing the volume fraction of one phase within each computational cell. This is done through the solution of a pure advection equation for the discontinuous field $F(\boldsymbol{x}, t)$,

$$\frac{DF}{Dt} = \frac{\partial F}{\partial t} + \boldsymbol{u} \cdot \boldsymbol{\nabla} F = 0. \tag{51}$$

The Navier–Stokes equations are solved in the entire computational domain, with the local values of density and viscosity calculated from the volume fraction, namely

$$\begin{aligned} \rho(\boldsymbol{x}, t) &= F(\boldsymbol{x}, t)\, \rho_w + (1 - F(\boldsymbol{x}, t))\, \rho_a, \\ \mu(\boldsymbol{x}, t) &= F(\boldsymbol{x}, t)\, \mu_w + (1 - F(\boldsymbol{x}, t))\, \mu_a. \end{aligned} \tag{52}$$

Numerical diffusion is usually introduced in the numerical solution of this problem, leading to a lack of definition of the interface which may be smeared over many cells. When adequate conservative schemes for updating the volume fraction are used, the VOF method behaves well with respect to mass conservation [15]. On the other hand, the interface curvature, which is critical in some application (e.g. when surface tension effects are relevant), is difficult to estimate from the volume fraction distribution.

The Level Set method is based on the construction of a smooth function ϕ, defined in the whole computational domain as the signed distance function from the interface: negative values correspond to one fluid, positive values to the other. The zero level set of ϕ represents the interface. The interface is determined by solving the following advection equation for ϕ:

$$\frac{\partial \phi}{\partial t} + \boldsymbol{u} \cdot \boldsymbol{\nabla} \phi = 0. \tag{53}$$

The property of ϕ being a distance function is not preserved during advection. It has been shown [22] that a reinitialization procedure is necessary in order to restore this property to the level set function, at least in regions close to the interface and that this procedure enhances the performance of the numerical algorithm.

The *reinitialization* consists in constructing a new function $\phi(\boldsymbol{x})$, with the property that its zero level set is the same as $\phi_0(\boldsymbol{x})$ (ϕ_0 now denotes the solution to (53)) and such that ϕ is the signed distance function from the interface. This problem can be formulated as follows:

$$\begin{cases} \text{Find } \phi \text{ such that} \\ \\ |\boldsymbol{\nabla} \phi| = 1, \\ \\ \phi|_\Gamma = 0, \end{cases} \tag{54}$$

where $\Gamma = \{\boldsymbol{x} \in \Omega : \phi_0(\boldsymbol{x}) = 0\}$ is the interface.

Different reinitialization procedures have been proposed in literature, see e.g. [22,2]. The most common, introduced by Sussman *et al.* in [22], requires the solution of the following Hamilton-Jacobi equation to steady state

$$\begin{cases} \dfrac{\partial \phi}{\partial \tau} + \boldsymbol{w} \cdot \boldsymbol{\nabla} \phi = S(\phi_0), \\ \\ \phi_{|\tau=0} = \phi_0 \end{cases} \tag{55}$$

where $\boldsymbol{w} = S(\phi_0) \boldsymbol{\nabla} \phi / |\boldsymbol{\nabla} \phi|$, S is the sign function and τ is a pseudo-time.

The Navier–Stokes equations (1)-(3) around sails reduce to:

$$\partial_t \boldsymbol{u} + \boldsymbol{\nabla} \cdot (\boldsymbol{u} \otimes \boldsymbol{u}) - \frac{1}{\rho_a} \boldsymbol{\nabla} \cdot \boldsymbol{T}(\boldsymbol{u}, p) = \boldsymbol{g} \tag{56}$$

$$\boldsymbol{\nabla} \cdot \boldsymbol{u} = 0, \tag{57}$$

for $\boldsymbol{x} \in \Omega$, $t > 0$, being ρ_a the constant density of air.

These flow equations are coupled with equations like those in (26)-(27) for the sail deformation, possibly reduced to a simpler two-dimensional stress model as described in section 3.4. The coupling conditions are those on the velocity field and normal stresses illustreted in (29)- (30).

To solve such a complex problem, the numerical solution of the equations that govern the flow motion should be iteratively coupled with a mathematical model that compute the structural deformations. To date, a numerical method able to simulate correctly and efficiently in reasonable time the dynamics of the complete fluid-structure interaction problem on complex configurations such as the one of an America's Cup yacht is not available.

As a matter of fact, after space and (implicit) time discretization of both sets of equations (those for the fluid and those for the sail structure) plus the coupling equations, we could end up with a nonlinear system which, in compact form, reads:

$$N(\boldsymbol{\Phi}(t)) := \mathcal{S} \circ \mathcal{F}(\boldsymbol{\Phi}(t)) - \boldsymbol{\Phi}(t) = 0 \qquad \text{on } \Gamma_0^I, \tag{58}$$

for all $t > 0$. The resolvant operators $\mathcal{S}$ and $\mathcal{F}$ have the following meaning. For any given deformation $\boldsymbol{\Phi}$, $\mathcal{F}(\boldsymbol{\Phi})$ returns the solution $(\boldsymbol{u}, p)$ of the flow equations (56) -(57) on a domain external to the sail whose deformation is $\boldsymbol{\Phi}$, and with a Dirichlet boundary condition (29) for $\boldsymbol{u}$. On its turn, the operator $\mathcal{S}$ applied to the flow field $(\boldsymbol{u}, p)$ returns the deformation $\boldsymbol{\Phi}$ of the sail that satisfies equation (26) under the equilibrium condition on normal stresses at the sail skin (30). Should (26) be replaced by a two-dimensional shell model, the stress equilibrium condition will transform in a forcing (source) term for the shell equations.

The fixed-point equation (58) suggests the (obvious) fixed-point iteration procedure

$$\boldsymbol{\Phi}^{n+1} = \mathcal{S} \circ \mathcal{F}(\boldsymbol{\Phi}^n), \qquad n \geq 0, \tag{59}$$

that implies, at each iteration step n, the solution of the flow problem followed by one for the sail deformation. Note that a new grid should be generated on the deformed flow domain before undertaking the next flow computation.

When looking for a steady-state solution, the fluid-structure interaction problem (58) reduces indeed to a problem of *shape determination*, namely the problem of determining the shape of the sail at equilibrium. This implies that we get rid of time derivatives in equations (56) and (26). Moreover, the dynamic equation (29) simplifies to

$$\mathbf{\Phi}(\boldsymbol{\xi}, t), t) = 0, \quad (\boldsymbol{\xi}, t) \in \Gamma_0^I \times \mathbb{R}^+, \tag{60}$$

which implies that in iteration (59) the solution of the flow step $\mathcal{F}(\mathbf{\Phi}^n)$ depends on the sail domain but not on the rate of deformation of the sail.

In more complex situations (for instance the unsteady case), fixed-point iterations do not converge due to their staggered character. In these cases the Newton–Rapson method could be the matter of choice for facing successfully the intricacy of the coupled problem (58). Then, at any time step t^n, Newton iterations entail the solution of the following substeps:

(1) set $\mathbf{\Phi}_0^{n+1} = \mathbf{\Phi}^n$; then, for $k \geq 0$:
(2) solve $\mathcal{J}(\mathbf{\Phi}_k^{n+1})\, \delta\mathbf{\Phi}_k = -N(\mathbf{\Phi}_k^{n+1})$,
(3) set $\mathbf{\Phi}_{k+1}^{n+1} = \mathbf{\Phi}_k^{n+1} + \omega_k\, \delta\mathbf{\Phi}_k$, for a suitable $\omega_k > 0$.

The critical step is of course the computation of the Jacobian and the solution of the associated linear system (typically by GMRES iterations). In view of (58), we have

$$\mathcal{J}(\mathbf{\Phi}_k^{n+1}) \cdot \mathbf{\Psi} = \mathcal{S}'(\mathcal{F}(\mathbf{\Phi}_k^{n+1})) \circ \mathcal{F}'(\mathbf{\Phi}_k^{n+1}) \cdot \mathbf{\Psi} - \mathbf{\Psi}, \tag{61}$$

where $\mathbf{\Psi}$ is a solid state perturbation. Replacing the linearized flow operator $\mathcal{F}'$ and/or structure operator $\mathcal{S}'$ by inexact ones (based on either algebraic manipulations or on the use of simplified physical models) leads to inexact Newton methods. On the latter cases a wise choice of the parameter ω_k (based, *e.g.*, on line search or on Aitken extrapolation techniques) might reveal mandatory in order to achieve convergence (see, *e.g.*, [17]).

5 Devising hierarchical models to reduce complexity

The partnership with Alinghi gives EPFL scientists a unique opportunity to apply immediately many of their basic research findings. As a matter of facts, the techniques that have been used and the analyses which have been carried out share many analogies with those applied in completely different domains, such as, e.g., parallel numerical algorithms for external aerodynamics in aerospace engineering, environmental or physiological flow modeling.

As pointed out in Section 4, the complete problem based on the coupling between Navier–Stokes equations with free-surface and the equations for structure deformation has a prohibitive complexity. This has called for employing a series of models (or problems) of lower complexity and to properly (and quickly!) integrate them in the design process.

Solving the complete problem by neglecting the deformability of the structure is the first assumption that can be made in order to reduce the complete model. By so doing, we are left with a problem which accounts "only" for the fluid components, namely the flow in the water, the one in the air, and their interaction at the waterline level (the free-surface), where waves are generated.

The approximate solution of this problem demands for robust and accurate numerical algorithms that should be implemented on computers capable of carrying out many billions of operations per second. However, solving accurately these equations is well rewarding as the results that are obtained can be used to simulate all tiny details of the flow field around the boat and the sails. Many different kinds of boat configurations (e.g. different hulls, keels, bulbs or winglets) have been simulated in both upwind and downwind sailing regimes. Moreover, several kinds of atmospheric conditions have been accounted for by properly changing the initial and boundary conditions for the Navier–Stokes equations. More precisely, as previously noted, what we have solved are the RANS equations, which are obtained from the original Navier-Stokes equations by taking suitable ensemble averages and using appropriate models to describe the Reynolds turbulence stresses.

Although simplified by having neglected the structural deformations, yet everyone of these simulations has a tremendous computational complexity, as it requires:

- translate a new configuration provided by the design team into its geometrical description (using hundreds of patches of little surfaces);
- generate the grid around the boat consisting of hundreds of thousands of triangles and quadrilaterals (see Fig. 3);
- generate the volume grid composed of tetrahedra and exhaedra to fill the three-dimensional computational flow domain;
- solve the the RANS equations by parallel computers in the computational domain.

This leads to the solution of nonlinear (fully coupled) algebraic systems with up to 30 millions (or more) of unknowns by iterative procedures.

Two different types of computer systems have been used to perform the dif-

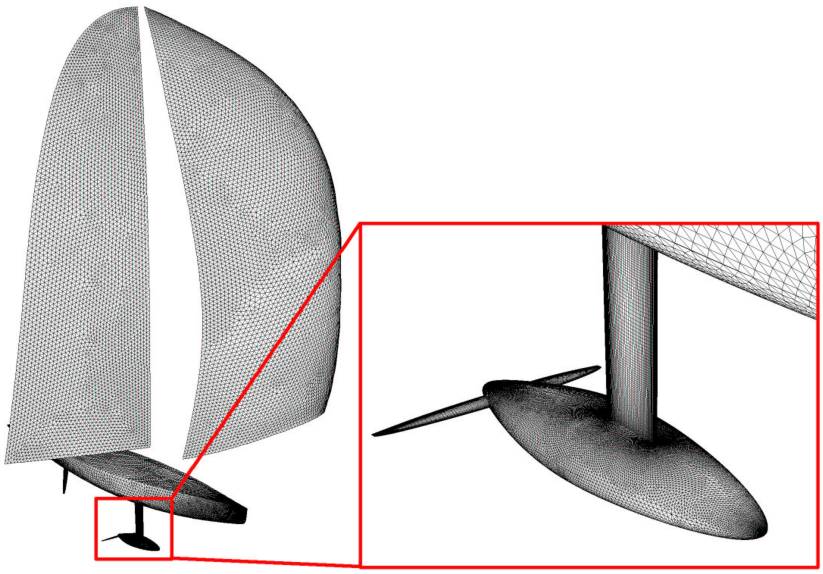

Fig. 3. Surface grid for an IACC yacht.

ferent simulation tasks:

- a desktop workstation with two Intel Pentium 4 (1.7 GHz) processors and 2 GB memory (for the pre-processing and the post-processing),
- an SGI Origin 3800 central computer system with 128 MIPS R14000 (500 MHz) processors and 64 GB memory (for the solution of the Navier-Stokes equations).

Concerning volume grid generation, to capture the high gradients in the boundary-layer region close to the body, an anisotropic prismatic grid is extruded from the wall surface grid. The first layer spacing, stretching and thickness of this grid region are dictated by the Reynolds number, the turbulence model, and the method used to resolve the inner region of the turbulent boundary layer. The volume grid generation is then completed by filling the external volume with tetrahedrons.

The grid sizes and computational times for a typical simulation in two sailing conditions (upwind and downwind) are indicated in Table 1. The computational times are quoted for 16 processors of the SGI Origin 3800 computer system. The grid generation process requires a considerable effort in generating the computational grid. Table 2 indicates the engineer and computer time and required for the generation of a typical grid.

Table 1
Mesh sizes and computational times

Configuration	**Downwind**	**Upwind**
Geometry	Hull/Keel/Wlets	Hull/Keel/Wlets/Rudder
Surface mesh	180,000 faces	200,000 faces
Volume mesh	4,500,000 elements	5,500,000 elements
Runtime	8 hr	10 hr

Table 2
Estimates of mesh generation time requirements

Mesh Generation Step	**Engineer time**	**Computational time**
Geometry repair	15 min - 3 hr	5 min
Surface meshing	40 min	5 min
Boundary layer extrusion	15 min - 1 hr	15 min
Tetrahedral meshing	20 min	15 min
Total	1.5 hr - 5 hr	40 min

5.2 Further simplified models

The results obtained from our simulations have been analyzed by the design team, compared and combined with those obtained by experimental analyses (in the wind tunnel or in watertank) or by the computer using even more simplified models which can be run in real time on a simple personal computer. These simpler methods are usually based on potential flow (where fluid viscosity is neglected as well as vorticity creation and propagation). They can provide fast valuable information (surface pressure and global forces) for non-separated flows such as the hydrodynamic flow around boat appendages and the aerodynamic flow around upwind sailing configurations. The results obtained by RANS models have been integrated into the overall design process, in particular with the results coming from different computational tools mainly used in the Alinghi design team. They include:

- a free-surface potential flow panel code (Splash^{TM}) for aero/hydrodynamic design and analysis, to provide the free-surface location to be used then in the RANS solver, the latter being applied separately on the two subdomains Ω_w and Ω_a;
- a 2D boundary layer solver (XFoil^{TM}) and a 3D boundary layer solver (3C3D^{TM}) for non-separated flows, to compute the location where the transition from laminar to turbulent flow regime does occur. This information is then used in the RANS solver to identify the subregions of the domain in which the turbulence model should be switched on;

- a potential flow panel code (Flow-MemBrain^{TM}) for fluid-structure simulations of sails, to create the deformed sails geometry used afterward in the RANS simulations.

6 Numerical simulations

Our numerical simulations have concerned three main subjects of research: the analysis of different appendages configuration for a IACC yacht, the free-surface flow around the hull and its interaction with the appendages and, finally, the aerodynamic flow around the sails [3]. These calculations were used to supply a large variety of information to the design team for integration into various stages in the design cycle.

Extensive post-processing efforts were targeted at calculating component forces and visualization of the local fluid flow near specific regions of interest. This information was used to help the designers make shape variations, even in the late stages of appendage component design.

6.1 "Optimization" of the appendages

A key factor for the success of an America's Cup yacht is the design of a set of appendages which can guarantee high performances in different sailing configurations (upwind and downwind) over a large range of wind conditions (and, consequently, of boat speeds). On one hand, the drag should be minimized in order to obtain the highest downwind speed, on the other hand, in upwind sailing, the efficiency (lift/drag) should be maximized. Other factors, such as heeling stability and structural resistance constraints, must be taken into account as well.

A broad variety of different appendage configurations have been analyzed. The flow around the hull and a full set of appendages common to IACC racing yachts (including keel, bulb, winglets, and rudder) has been simulated. Due to the complexity of modelling the free surface a static water surface was assumed for the appendage studies, with a free-slip boundary condition placed at the waterplane.

The design parameters defining a bulb shape include the lateral and vertical profiles and the cross section. Advantages and disadvantages of slender (long) versus fuller (short) bulb shapes have been assessed by testing different configurations. Longer bulbs usually perform better with respect to the pressure drag, on the other hand they have larger wetted surface which increase the

viscous component of the drag. The influence of different cross section shapes has also been investigated. In particular, we have analyzed the influence of lowering the center of gravity by using cross sections of the bulb more elliptical than traditional shapes with the long axis running port-starboard. The potential advantage is that a lower center of gravity increases the righting moment of the yacht. Also in this case, the numerical simulation of several bulbs with different cross sections has given useful indications about the tradeoff between advantages and disadvantages of each configuration. Other characteristics, such as the bulb camber and the shape of the tail region, have been analyzed as well (Fig. 4).

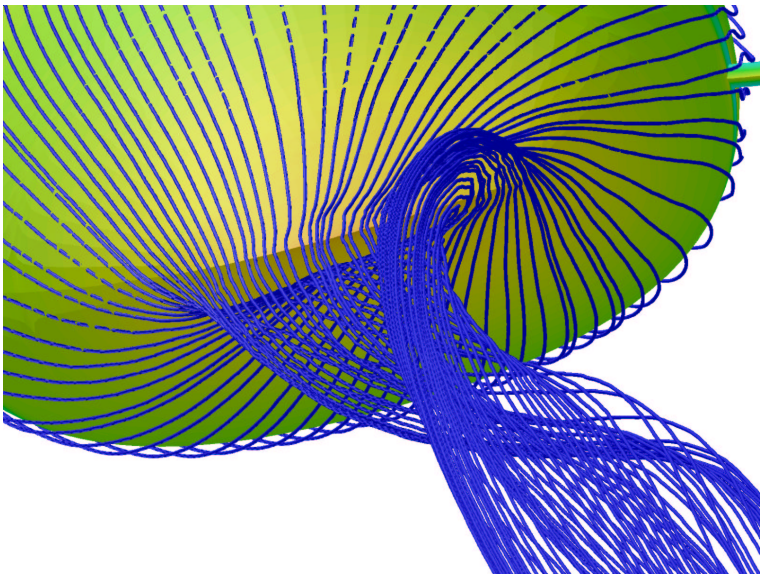

Fig. 4. Streamlines showing the vortex detaching from the bulb tail.

As concerns the keel, numerical simulations have been performed in order to compare different sections and planform shapes (Fig. 5).

Since 1983, when they were first adopted by the America's Cup winner Australia II, winged-keels have been extensively employed in IACC yacht design. Similarly as in aircraft applications, the underlying idea is that the presence of winglets at the tip of a keel (or an aircraft wing) can reduce the lift-induced drag C_{D_i} which is defined as

$$C_{D_i} = \frac{C_L^2}{\pi \Lambda_{\text{eff}}} \tag{62}$$

where C_L is the lift coefficient and Λ_{eff} is the effective wing aspect ratio. Indeed, this reduction is given by the increase of Λ_{eff} when winglets are employed. Moreover, in a sailing boat, winglets can also provide some trust (negative drag) when the boat pitches and heaves in waves. In spite of their extensive use in the last 20 years, an optimal winglet design still remains an open problem in the yacht design community.

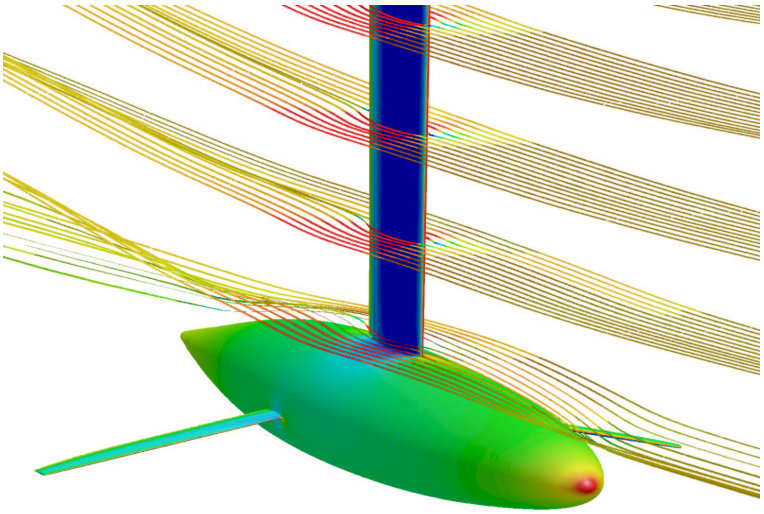

Fig. 5. Surface pressure contours on the yacht appendages and streamlines around the keel.

Several winglet design parameters have been considered in the present work: longitudinal position, angle of attack, twist and sweep angles (Fig. 6). The results that can be extracted by those simulations are both quantitative (forces, pressure coefficient distributions, wall stress distributions) and qualitative (vector fields and streamlines visualizations to locate, e.g., regions with flow separations).

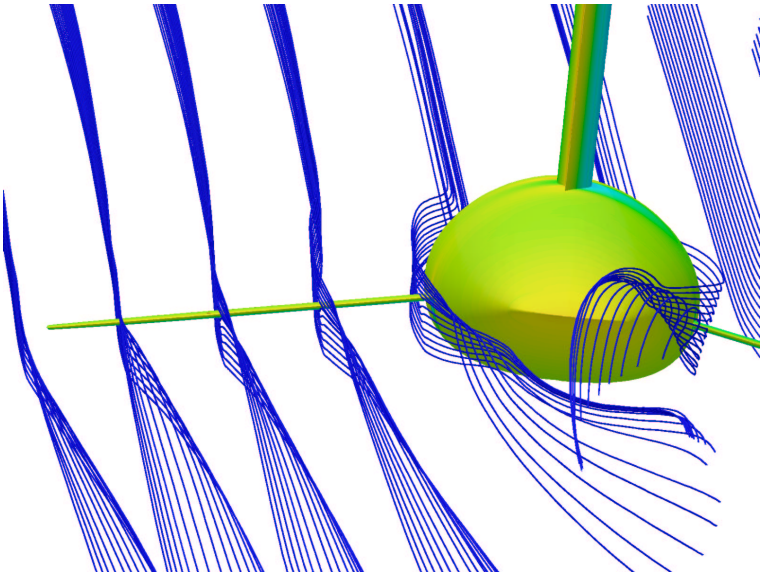

Fig. 6. Surface pressure contours on the yacht appendages and streamlines around the winglets.

For America's Cup yachts, the wave drag can be a significant fraction of the total hull resistance, as much as 60% at 10 knots of boat speed in downwind sailing. An accurate determination of this component is important when comparing the performances of two very similar hulls. Recent America's Cup efforts have shown an emphasis on delaying the sharp rise in the drag vs. hull-speed curve by shaping the ends of the boat in a way that increases effective length without a penalizing increase in measured length. These local geometric modifications require accurate experimental and numerical investigations to predict correctly the performance differences deriving from these subtle changes. In a typical hull design process, the naval architects will run a matrix of hull shapes through a fast free surface potential solver to determine a set of candidates to be tested in the towing tank. Force coefficients from both the panel code (e.g., Splash^{TM}, see [20]) and experimental results are fed into a Velocity Prediction Program (VPP) to calculate round-the-buoys performance deltas versus a baseline configuration. RANS-based simulations can be incorporated into this process in a number of ways. They can be used to decrease the number of candidate shapes for which models are constructed and tested in the towing tank. They can also be used to evaluate the free-surface flow in situations where panel codes are unable to resolve critical differences arising from viscous effects. A first example is the study of stern shapes where the boundary layer and flow separation in the stern region result in an effective lengthening of the hull that alters the drag due to wave making. A second example is the optimization of the tradeoff between wave and friction drag associated with the addition of volume to the bow region, a current trend in IACC design.

In the present work, we have investigated the effect of this increase in forward volume by comparing different hull designs. In particular, a specific bow shape study has been performed to help determine the range of boat speed for which an increase in forward volume is beneficial (see Fig. 7 and 8).

In upwind sailing, the pressure distribution on the keel has a strong interaction with the free-surface, in particular on the windward side of the hull, where the suction side of the keel is closer to the free-surface. One method of decreasing this interaction, thereby reducing any drag deriving from this interference, is by increasing the distance between the keel load and the free-surface. In the present work, the effect of lowering the load center of the keel by altering its taper ratio (tip chord/root chord) has been investigated (see Fig. 9).

The free-surface computations presented here have been carried out using a grid conforming Navier–Stokes solver based on finite volume spatial discretization (see, for details, [4]).

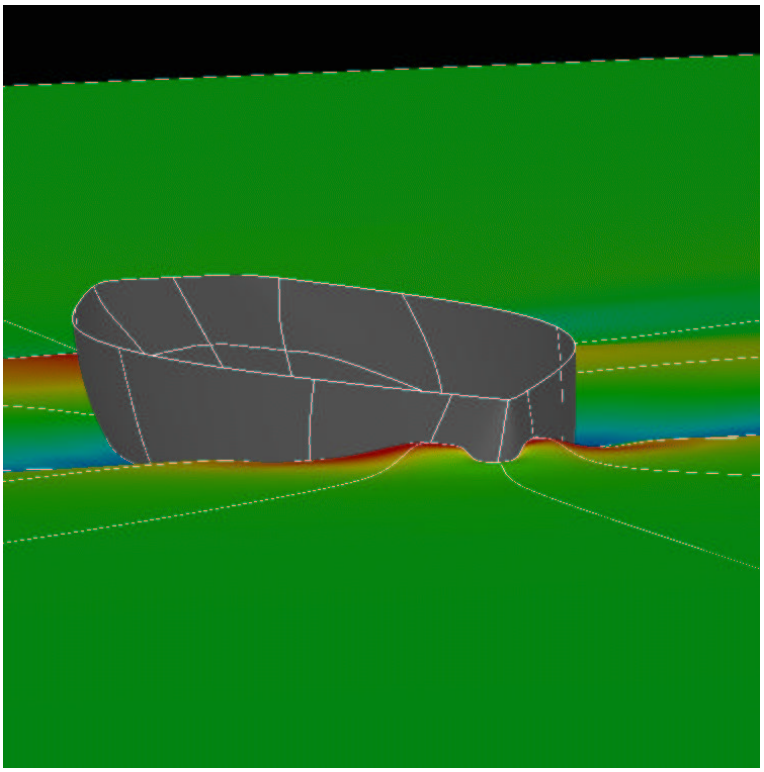

Fig. 7. Wave elevation around a IACC yacht sailing downwind at 10 knots.

6.3 Aerodynamics of sails

In downwind sailing, there are significant regions of separation on the main sail and the spinnaker resulting from the large angle of attack. The design of downwind sail shapes and their optimal trimming remain a critical element in the search for speed gains in the America's Cup.

The present study concentrated on the numerical simulation of the flow around downwind sailing configurations. Three specific aspects of downwind sailing aerodynamic simulation have been considered: calculation of forces, two-boat interaction, and the evolution of the wind shadow.

6.3.1 Downwind Sail Forces

The geometries used in this set of simulations include the exposed hull, mainsail, symmetrical spinnaker, and appendages. Appropriate values of the flow conditions (sailing angle, true wind speed and hull speed) were prescribed.

Both the hydrodynamic and aerodynamic regions were modelled. The primary purpose of including both the hydrodynamic and aerodynamic components was to provide a first approximation for solving the fully-coupled aero-

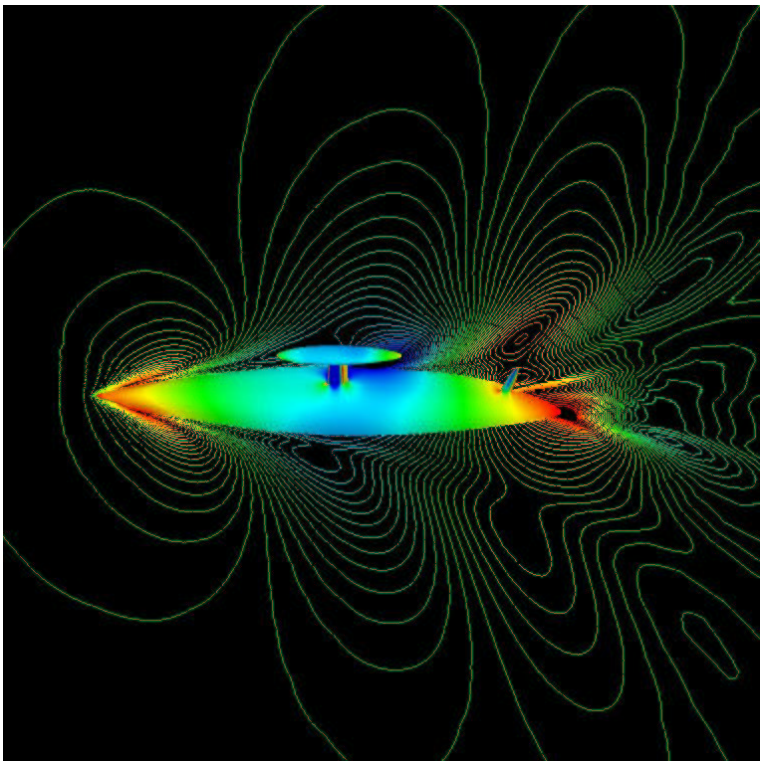

Fig. 8. Wave elevation around a IACC yacht sailing upwind at 10 knots.

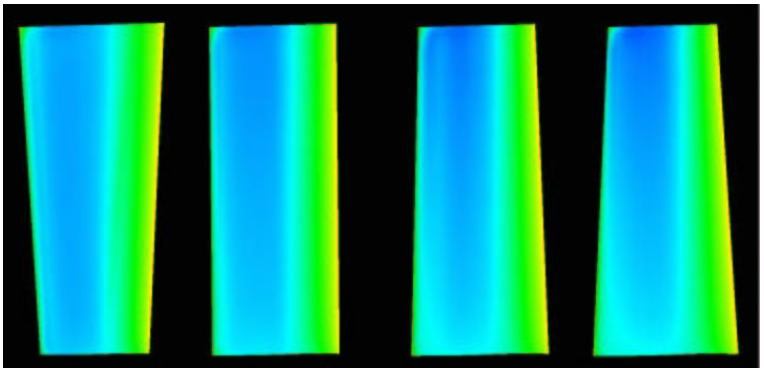

Fig. 9. Surface pressure contours on four keels with different taper ratio

hydrodynamic system. In the present case, the evolution of the free-surface is neglected and a symmetric boundary condition is imposed on the flat static waterplane. With the addition of both a free surface and a dynamic motion of the geometry in response to the forces in an iterative process, it should be possible, as a future possible development, to construct a simplified VPP based on the RANS equations.

The surface grid on the whole boat geometry and the surface pressure distribution are displayed in Fig. 3 and 10. For this simulation, a boat speed of 10 knots, true wind speed of 15 knots and true wind angle was 160 degrees have been considered.

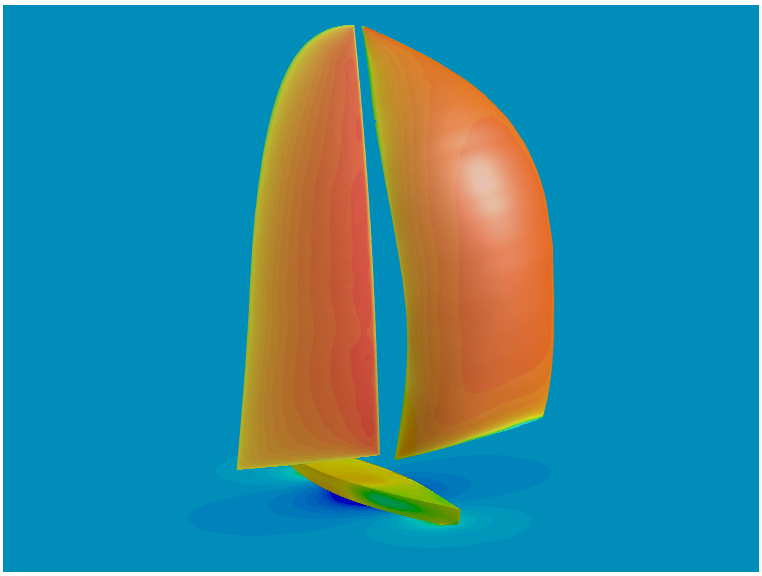

Fig. 10. Surface pressure distribution for a IACC yacht sailing downwind.

Based on an analysis of the driving and side forces, as well as an examination of the region of separation, the sails appear to act as a combination of a parachute (with the lift aligned with the direct of thrust) and a vertical wing (drag aligned with the direction of thrust), as observed by Richards in [19].

6.3.2 Two-Boat Simulations

The physics underlying the tactical advantage of the safe leeward position in upwind sailing are well understood and are often treated in textbooks on sail trim and tactical sailing [25]. Downwind match racing tactics are dominated by downwind covering, or "blanketing", which is governed by more complex fluid dynamics. The large-scale regions of complex vortical flow leaving the windward yacht interact with the wind gradient and manifest themselves in a perturbation of the freestream conditions, which can adversely affect the progress of the leeward yacht. This perturbation is known as the *wind shadow*.

Two boats sailing in a downwind coverage situation have been simulated to provide a detailed view of their interaction through aerodynamic shadowing. Rather than examine the properties of the wind shadow and indirectly deduce its potential influence on another boat, the addition of a second boat in the simulation allows this influence to be directly determined. By choosing two identical boats, the influence of the different flow fields experienced by each boat can therefore be assessed. In reality the boats will have their sails trimmed differently to the different wind conditions. In the absence of fluid-structure effects in the simulation, this more detailed interaction cannot be accounted for.

The wind speed and angle over the full extent of the sails of the two boats

greatly change. This results in a significant change in the aerodynamic forces exerted on the leeward boat's sails. The pressure on the windward surface of the two boats' sails is found to be substantially different both in magnitude and in spatial distribution leading to a significant difference in the driving forces of the two configurations. Some of this difference would normally be compensated by an alteration of the sail trim of the leeward boat.

A visual indication of the perturbed flow encountered by the leeward yacht is shown in Fig. 11.

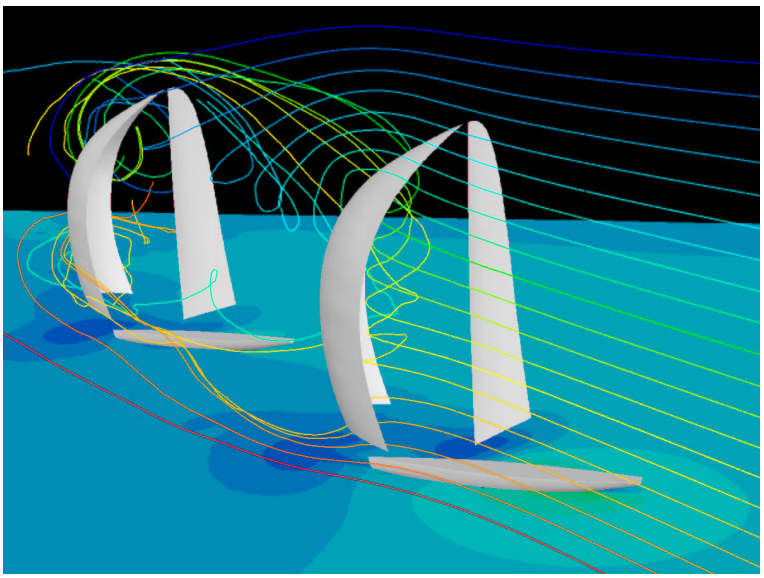

Fig. 11. Aerodynamic interaction between two boats sailing downwind.

6.3.3 Wind-shadow evolution

A more detailed analysis of the wind shadow region behind an IACC yacht sailing downwind has been performed by simulating the flow around the exposed part of the hull, mainsail and symmetrical spinnaker. The inflow boundary conditions on the velocity take into account the presence of the atmospheric boundary layer. Because the hull was stationary in the simulation, the variation in both the magnitude of the apparent wind and the apparent wind angle was prescribed. This was derived from the boat speed, sailing angle, and a relation for the true wind speed obtained from an approximation of the atmospheric boundary layer. For this study, the so-called 1/10 law was used to model the true wind speed TWS in this layer,

$$TWS(z) = TWS(10)\left(\frac{z}{10}\right)^{\frac{1}{10}} \tag{63}$$

where z is the vertical coordinate in meters measured from the static waterplane.

A qualitative assessment of the simulation results reveals the flow to be dominated by the two trailing vortices generated at the head and base of the spinnaker and mainsail. These vortices extend many boat lengths and can provide a significant influence on the aerodynamic forces exerted on the downwind boat. To localize the shadow region, an indicator that can be used is the *defect velocity*

$$\sqrt{(u_x - u_{bcx})^2 + (u_y - u_{bcy})^2 + u_z^2}$$

where $\boldsymbol{u}_{bc} = (u_{bcx}, u_{bcy}, 0)$ is the inflow boundary velocity.

An overview of the wind shadow produced by the boat is presented in Fig. 12, where contour plots of the defect velocity at different lateral planes are displayed. The propagation of the two trailing vortices downstream at different displacements, corresponding to different angles, is clearly observed.

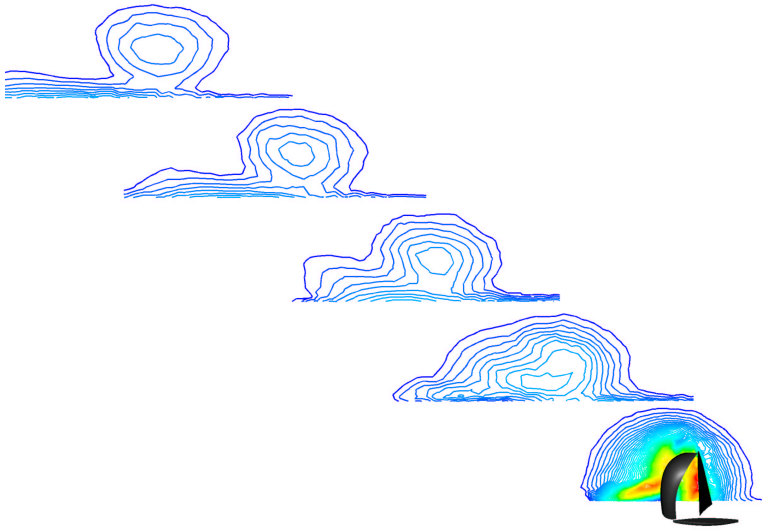

Fig. 12. Contours of defect velocity at different lateral distances showing the evolution of the wind shadow.

Information of this kind extracted from the simulations can support the tactical decisions of both the leading and trailing yachts to maximize coverage or minimize its damaging effects.

7 Conclusions

The mathematical models describing the different aspects that characterize the hydrodynamic and aerodynamic flows around a sailing yacht have been presented and discussed.

The equations governing two-fluids incompressible flows have been introduced together with suitable interface conditions associated to the evolution of the

free-surface interface between air and water. We have presented the derivation of the Reynolds Averaged Navier–Stokes (RANS) equations for the considered problem and an adequate model for the turbulent Reynolds stresses. The interaction between air flow and sail structures has also been considered and a formulation of the fluid-structure interaction problem has been proposed. We have also discussed the discretization methods for the approximation of the flow equations as well as the techniques for the fluid-structure interaction.

The numerical simulations performed in the framework of the collaboration between the EPFL and the Alinghi Design Team have been presented, highlighting the role of Computational Fluid Dynamics simulations based on RANS equations and their integration in standard yacht design process. We have considered a hierarchy of computational tools characterized by different levels of validity, complexity, computational cost, ease of use and acceptance within the design community, describing the possible mutual interactions between them.

Acknowledgments

The authors would like to acknowledge Geoffrey W. Cowles and Mark L. Sawley for their contribution in the research activity on which the present paper is based. The members of the Alinghi Design Team, and in particular Grant Simmer, Jim Bungener and Manolo Ruiz de Elvira, are also acknowledged for their precious support and their patience in explaining to us the various aspects of the racing yacht design procedure. We are grateful to Sylvia Anicic and Luca Formaggia for the useful discussions on the fluid-sail interaction problem. Jan-Anders Manson, coordinator of the EPFL/Alinghi partnership, is acknowledged for his inestimable ability in managing this exciting scientific challenge. The pictures reported in this paper illustrate simulations carried out using the commercial code FLUENT^{TM}and the research code SHIP107MB developed at Princeton University. This research has been supported by an EPFL grant.

References

[1] T. J. Barth and D. Kasper's The design and application of upwind schemes on unstructured meshes, Technical Report AIAA-89-0366, AIAA 27th Aerospace Sciences Meeting, Reno, Nevada, 1989.

[2] R. Codina and O. Soto A Numerical Model to Track Two-Fluid Interfaces Based on a Stabilized Finite Element Method and the Level Set Technique, Int. J. Num. Meth. Fluids, 40, 293–301, (2002)

[3] G. W. Cowles, N. Parolini and M. L. Sawley, Numerical Simulation using RANS-based Tools for America's Cup Design, in: Proc. 16th Chesapeake Sailing Yacht Symposium, Anapolis, Maryland, (2003).

[4] G. W. Cowles, A Viscous Multiblock Flow Solver for Free-Surface Flows past Complex Geometries, Ph.D. Thesis, 2001.

[5] J. R. Farmer, L. Martinelli and A. Jameson, A Fast Multigrid Method for Solving Incompressible Hydrodynamic Problems With Free Surfaces, AIAA Journal, 32(6), 1175–1182, (1993).

[6] B. R. Hutchinson and G. D. Raithby, A Multigrid Method Based on the Additive Correction Strategy, Numerical Heat Transfer, 9, 511–537, (1986).

[7] T. Hino, Computation of Viscous Flows with Free Surface around an Advancing Ship, in: Proc. 2nd Osaka Int. Colloquium on Viscous Fluid Dynamics in Ship and Ocean Technology, Osaka University (1992).

[8] C. W. Hirt and B. D. Nichols, Volume of Fluid (VOF) Method for the Dynamics of Free Boundaries, J. Comp. Phys., 39, 201–225 (1981).

[9] J. M. Hyman, Numerical Methods for Tracking Interfaces, Physica, 12D, 396–407 (1984).

[10] D. B. Kothe, Volume Tracking of Interfaces having Surface Tension in Two or Three Dimensions, AIAA Paper, 96-0859, (1981).

[11] P. L. Lions, Mathematical Topics in Fluid Mechanics: Incompressible Models, Oxford Lecture Series in Mathematics and Its Applications, 3, 1997.

[12] S. Osher and R. Fedkiw, The Level Set Method and Dynamic Implicit Surfaces, Springer-Verlag, New York, 2002.

[13] S. Osher and J. A. Sethian, Fronts Propagating with Curvature-Dependent Speed: Algorithm Based on Hamilton-Jacobi Formulationsi, J. Comp. Phys., 79, 12–49 (1988).

[14] S. V. Patankar, Numerical Heat Transfer and Fluid Flow. Hemisphere, Washington, D.C., 1980.

[15] J. E. Pilliot and E. G. Puckett, Second-Order Accurate Volume-of-Fluid Algorithms for Tracking material interfaces, submitted to J. Comp. Phys..

[16] P. Mohammadi and O. Pironneau, Analysis of the k-epsilon model, Masson, Paris, 1994.

[17] A. Quarteroni, R. Sacco and F. Saleri, Numerical Mathematics, Springer, 2000.

[18] C. M. Rhie and W. L. Chow, Numerical Study of the Turbulent Flow Past an Airfoil with Trailing Edge Separation, AIAA Journal, 21(11), 1525–1532, (1983).

[19] P. J. Richards, A. Jonhson and S. Stanton, America's Cup Downwind Sails - Vertical Wings or Horizontal Parachutes?, J. Wind. Eng. Ind. Aerodyn., 89, 1565-1577, (2001).

[20] B. S. Rosen, J. P. Laiosa, W. H. Davis and D. Stavetski, Splash Free-Surface Code Methodology for Hydrodynamic Design and Analysis of IACC Yachts, in: Proc. 11th Chesapeake Sailing Yacht Symposium, Annapolis, MD, (1993).

[21] J. A. Sethian Level Set Methods and Fast Marching Methods, Cambridge University Press, 1999.

[22] M. Sussman, P. Smereka and S. Osher, A Level Set Approach for Computing Solutions to Incompressible Two-Phase Flow, J. Comp. Phys., 114, 146–159 (1994).

[23] G. Tryggvason, B. Bunner, A. Esmaeeli, D. Juric, N. Al-Rawahi, W. Tauber, J. Han, S. Nas and Y.-J. Jan, A Front-Tracking Method for the Computations of Multiphase Flows, J. Comp. Phys., 169, 708–759 (2001).

[24] M. Vogt and L. Larsson, Two Level Set Methods for Predicting Viscous Free Surface Flows, in: Proc. 7th International Conference on Numerical Ship Hydrodynamics, Nantes, (1999).

[25] T. Whidden, The Art and Science of Sails, St. Martins Press, New York, 1990.